Optics & Laser Technology 139 (2021) 106978

Contents lists available at ScienceDirect

Optics and Laser Technology

journal homepage: www.elsevier.com/locate/optlastec

Full length article

High performance and tunable optical pump-rejection filter for quantum photonic systems

Giuseppe Brunetti, Nicola Sasanelli, Mario N. Armenise, Caterina Ciminelli *

Optoelectronics Laboratory, Politecnico di Bari, Via Orabona, 4, 70125 Bari, Italy

ARTICLE INFO

Keywords:
Tunable filters
Ring resonators
Mach-Zehnder Interferometers

ABSTRACT

Integrated photonic circuits have become an attractive platform for the quantum information processing, paving the way for quantum information management with scalable device. In this context, silicon photonics represents the most mature technology to implement the quantum system functionalities, due to its large scalability and compatibility with *CMOS* technology. Efficient photon-pairs sources based on Spontaneous Four-Wave Mixing (*SFWM*) and high-performance photodetector have been already demonstrated. The efficient detection of photon-pairs requires a pump filter at the photodetector, preserving the signal-idler pair. Thus, filters with high Extinction Ratio (*ER*), low Insertion Loss (*IL*) and narrow rejection Bandwidth (*BW*) are needed. Here, we propose the design of an ultra-high-performance rejection filter, based on a silicon dual-loaded single input/output Mach-Zehnder Interferometer (*MZI*), with one branch coupled to a Ring Resonator (*RR*) and the other to three serially coupled *RRs* forming a Coupled Optical Resonator Waveguide (*CROW*). Very high performance (*ER* = 150.55 dB, *IL* = 0.104 dB, *BW* = 0.243 nm), within a footprint of 60 μm × 160 μm, has been calculated, demonstrating its suitability for an efficient suppression of the pump signal. The filter response is also thermo-optically tuneable in a 6 MHz range, with a reconfigurability time of about 8 μs.

1. Introduction

Currently quantum information processing is a hot R&D topic in the Quantum Science, aiming at exploiting light states to enhance speed, versatility, and performance of quantum information systems smaller and smaller in size [1–3]. During the last decade, integrated quantum photonics has emerged as a promising technology for realizing high performance systems in small footprint [4], overcoming the issues of the early stage quantum systems based on optical devices with bulky configurations [5]. Quantum integrated photonic circuits secure several key advantages, such as easily reconfigurable architectures, enhanced light-matter interaction, small system footprint, high stability of optical elements and interfacing with *CMOS* electronics. In this context, the silicon photonics results very attractive to implement key functionalities in a quantum integrated system, as generation, manipulation and detection of photons [6].

High efficient production of quantum-correlated photons pairs through *SFWM* and a silicon ring resonator has been demonstrated, with relatively good characteristics in terms of small footprint and enhanced light intensity [7–8]. Photon-pair generation via *SFWM* involves pumping a non-linear medium with a high power laser [9]. By exploiting χ^3 in silicon, signal-idler pair can be generated, spectrally interleaved by the pumped beam that, of course, has to be efficiently filtered out [10] to preserve the single-photon pair. A narrow rejection bandwidth (<1 nm) is also required to allow short signal/idler separation, and then, to minimize the dispersion effects that could affect the *SFWM* efficiency.

Rejection function has been performed by off-chip solutions [6,11–13], based on Wavelength Division Multiplexing (*WDM*) modules, Fiber Bragg Gratings (*FBGs*) or monochromators, with large *ER* (>80 dB) in a large volume, that collides with the system scalability.

During the last few years, a great research effort has been spent on the design of integrated pump filters [14], mainly based on Bragg gratings (*BGs*) [15–18], contra-directional couplers [20–21], and Mach-Zehnder Interferometers (*MZIs*) [10,22].The wavelength selective nature of the 1D-photonic crystals makes the Bragg gratings as the simplest solution to perform high pump suppression. Large *ER* values (>60 dB) has been experimentally demonstrated for Silicon on Insulator (*SOI*) corrugated waveguide, but with large footprint (≈ 1 mm^2) and *BW* ≫ 1 nm [15]. Although the *ER* appears to be very promising, the very large index contrast of the *SOI* platform clashes with the small bandwidth

* Corresponding author.
E-mail address: caterina.ciminelli@poliba.it (C. Ciminelli).

https://doi.org/10.1016/j.optlastec.2021.106978
Received 3 December 2020; Accepted 27 January 2021
Available online 10 February 2021

requirement. In particular, corrugation widths of the order of tens of nm are required to meet the *BW* requirement that makes difficult the device fabrication. To overcome these issues, solutions based on sub-wavelength *BGs* have been proposed with $ER > 40$ dB, and $BW \approx 1$ nm [16]. A racetrack resonator with *BG* superimposed on a portion of the resonator path has been reported in [17], performing a $BW < 0.1$ nm with a small *ER* (>15 dB). Moreover, a broken-coherency multimode filter, that consists of cascaded multimode tilted BGs, has been proposed in [18], with an $ER > 80$ dB and a rejection *BW* of about 6 nm.

Contra-directional couplers have been also used for pump suppression in quantum photonic systems [19]. The cascade of contra-direction couplers showed high values of *ER* (>50 dB for 5 stages [20] and >70 dB for 16 stages [21]) with a complex fabrication process and a large footprint.

Complex configurations, based on cascaded *MZIs*, have recently demonstrated high *ER* values (>75 dB), but with $BW > 2$ nm and large footprint (order of mm^2). They also require an accurate control in the single steps of the fabrication process and an active tuning [10].

Pump rejection filters based on either resonant and non-resonant configurations have been also investigated, as simple ring resonators, *CROWs,* made by two ring resonators, and loaded and not-loaded *MZIs* [14]. Very narrow *BWs* (of the order of pm) and *ER* of about 50 dB have been simulated by using simple silicon *RRs*, which require an accurate control of the coupling gap between bus and ring [14]. *CROWs* have been proposed in literature to improve the *ER* with respect to the single *RR*. The cascade of two chips, each made by an all-pass 4th order *CROW*, has been reported in [23], experimentally demonstrating an $ER > 110$ dB with a rejection *BW* of 9 nm and a very large footprint (in the order of mm^2).

To improve the selectivity of the *MZI* device, also ring resonator loaded *MZIs* have been investigated [14], which show a significant improvement of the *ER,* with a wider *BW,* with respect to the single *RR*. However, *RR*-loaded *MZIs* perform a narrower *BW* with respect to *MZI* one, together with an *ER* worsening.

In order to obtain very large values of *ER* within a small rejection bandwidth, in this paper, we propose the design of a new pump rejection filter based on a dual loaded *MZI* in SOI technology. Very high performance, in terms of *ER*, *IL* and *BW* have been calculated in an extremely small footprint, together with the capability of thermo-optically tuning the filter response in a wide frequency range (≈ 6 MHz), making easier to lock the filtering shape to the pump resonance.

2. Design of the pump-rejection filter

The idea of this device was conceived to exploit the highly selective behaviour of *RRs* and the large suppression ratio of *MZI*. One branch of the dual-loaded *MZI* is coupled to a simple ring resonator and the other to three serially coupled ring resonators. The geometry of the ring resonators is such that it has the phase shift between the two branches equal to π. Under these conditions, $ER = 150.55$ dB, $IL = 0.104$ dB, and $BW = 0.243$ nm, with a very small footprint (60 μm × 160 μm), have been calculated, as explained in the following. The filter response can also be tuned in a wide frequency range (≈ 6 MHz), by exploiting the thermo-optic effect, so easily locking the filtering shape to the pump resonance. The proposed device, to our knowledge, shows the highest *ER* for on-chip pump filters, very narrow rejection bandwidth, very small size and the capability of tuning the filter response.

2.1. Device configuration

The proposed on-chip optical pump-rejection filter is sketched in Fig. 1(a). The light from a single source is split into two branches by using an integrated 1 × 2 Multi-Mode Interferometer (*MMI*). When the two waves propagating along the two optical branches experience a phase difference equal to π, a resonance spectrum can be obtained.

The waveguide we have designed (Fig. 1(b)) has a single-mode structure with a width $w = 500$ nm and a thickness $t = 220$ nm, fully embedded in silicon dioxide. The modal analysis of the designed waveguide has been carried out by using the effective index method [24]. Although in literature lower values of propagation loss are reported for the same waveguide [25], we assumed a propagation loss value $\alpha = 1$ dB/cm at $\lambda \approx 1550$ nm for the TE_0 mode to take into account potential loss contributions due to manufacturing.

The silicon *RR* with radius *R* shows a coupling centre-to-centre gap *g* (see Fig. 2(a)), while, *RRs* of the *CROW,* labelled as RR_i ($i = 1, 2, 3$) in Fig. 2(b), are spaced of g_1 between RR_1 and *MZI* arm, g_2 between RR_1 and

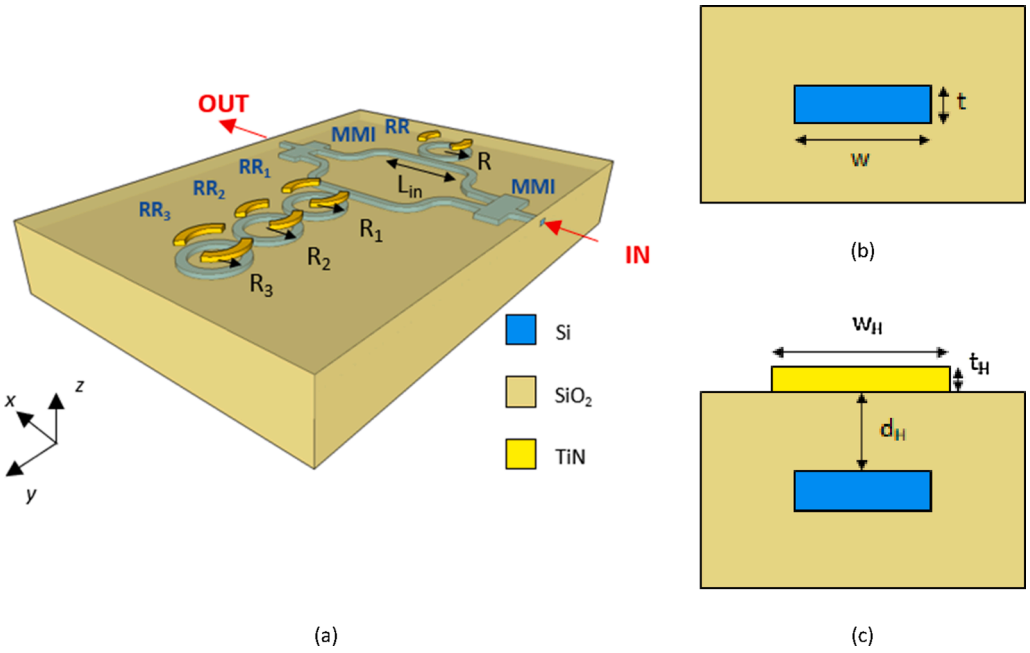

Fig. 1. (a) Configuration of the pump-rejection filter: the structure is fully embedded in silicon dioxide, made partially transparent in the figure, on the top of which TiN electrodes (in yellow) are placed; *R* is the radius of the single *RR*, R_1, R_2 and R_3 are the radii of the three *RR CROW*; L_{in} is the length of the *MZI* branches. (b) Silicon waveguide with thickness *t* and width *w*, embedded in silica; (c) Silicon waveguide with TiN electrode, t_H thick and w_H wide, d_H away from the silicon core.

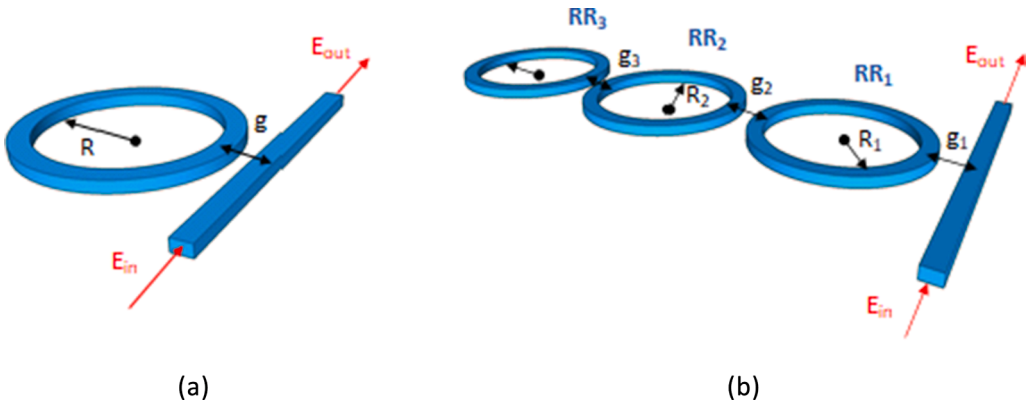

Fig. 2. (a) Silicon ring resonator with radius R and a coupling gap g; (b) *CROW* made by three serially coupled ring resonators RR_i (i = 1, 2, 3) with radii R_1, R_2 and R_3 and coupling centre-to-centre gaps g_1 (between bus – RR_1), g_2 (between RR_1 – RR_2) and g_3 (between RR_2 – RR_3).

RR_2, g_3 between the RR_2 and RR_3 (see Fig. 2(b)).

The 1x2 *MMI* has a configuration similar to that proposed in [26], which shows total optical loss of 0.005 dB within a very small footprint. The MMI consists of a multimode region 11.5 μm long and 3.6 μm wide, with tapered input/output sections. In order to avoid modal coupling between the two *MZI* arms [27], bent waveguides with a curvature of 10 μm have been considered cascading with 1x2 *MMI*. Thermo-optic effect has been considered to tune the filter due to its high tuning efficiency, response time of the order of μs and ease of fabrication [28–29]. A titanium nitride (TiN) electrode with thickness $t_H = 100$ nm and width $w_H = 500$ nm has been designed on top of *RRs* portions, spaced of $d_H = 1$ μm from the silicon core (Fig. 1(c)). To avoid that the tuning could affect the coupling efficiency, the electrodes are distributed outside the coupling regions, with same tuning lengths for all ring resonators. The tuning loss α_t [dB/m] have been also calculated.

2.2. Dual-loaded MZI

According to the *MZI* operation, a resonance results when the phase shift between the two optical beams travelling along the branches is equal to π. Therefore, the *RR* and the *CROW* have to be properly designed to achieve same attenuation along the *MZI* branches, resonances at the same frequency with a complementary phase shift, and same *ER*. Following these design criteria, we have optimized the performance of our device, achieving a narrow resonance with very high *ER*.

2.2.1. Single ring resonator load

Eq. (1) is the transfer function of the ring resonator coupler shown in Fig. 2(a)

$$T_{RR} = \left|\frac{E_{out}}{E_{in}}\right|^2 = \left|\frac{e^{i2\pi\beta R} - \tau}{\tau e^{i2\pi\beta R} - 1}\right|^2 \quad (1)$$

where the transmission coefficient is $\tau = \sqrt{(1\text{-}k^2)}$, with k the coupling efficiency, and β the propagation constant [rad/m] of the fundamental TE mode [30].

To assess the relationship between the coupling power efficiency $|k|^2$ and the centre-to-centre gap g, two-dimensional Beam Propagation Method (*2D-BPM*) simulations have been carried out [31], by taking also into account the ring curvature. The $|k|^2$ curves *vs.* g are reported in Fig. 3, for radius values $R = 10$ μm, 15 μm, and 20 μm. All curves show an inverse exponential trend with amplitudes strictly dependent on the RR curvature radius. A minimum radius of 10 μm has been taken into account to neglect the curvature losses, according to [25]. Parametric simulations have been carried out by varying g, and then, the coupling efficiency $|k|^2$, to estimate the *RR* performance parameters, i.e. the extinction ratio ER_{RR} and the bandwidth BW_{RR}. Furthermore, in order to

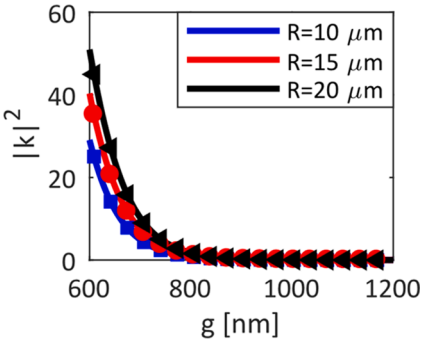

Fig. 3. $|k|^2$ *vs.* g for R = 10 μm, 15 μm and 20 μm.

define the phase response of the *RR*, useful to meet the phase conditions of the *MZI*, the phase at the ring resonator resonance (about 1550 nm), has been also calculated. As an example, the results for $R = 15$ μm are shown in Fig. 4(a-b). For the simulations, the gap g ranges from 600 nm to 1200 nm with a minimum step of 5 nm, by taking into account the manufacture feasibility. The BW_{RR}, ER_{RR}, and phase response trends, as it changes by g, are similar, but with different amplitudes, for all investigated radii (R = 10 μm, 15 μm, and 20 μm).

The maximum ER_{RR} value (≈ 36 dB, ≈ 51 dB, and ≈ 39 dB for $R = 10$ μm, 15 μm, 20 μm, respectively) has been observed at $|k|^2 \approx 0.137\%$ for $R = 10$ μm, $|k|^2 \approx 0.215\%$ for $R = 15$ μm, and $|k|^2 \approx 0.299\%$ for $R = 20$ μm. All these coupling conditions coincide with the critical coupling $|k|^2 = K_{critical}$ [32]. This value is strictly related to the ring resonator radius R and the propagation loss α. Since the total propagation loss ($\alpha \cdot 2\pi R$) is similar for all investigated radii (6.3×10^{-3} for $R = 10$ μm, 9.4×10^{-3} for $R = 15$ μm, 1.3×10^{-2} for $R = 20$ μm), the $K_{critical}$ values are very similar, too, and then, the critical coupling occurs at $g = g_{critical} \approx 900$ nm for all cases.

Although the critical coupling leads to high values of ER_{RR} (>30 dB), a small variation of g, also due to possible fabrication issues, heavily affects the performance (as an example, for $R = 10$ μm, an $ER_{RR} = 36$ dB has been calculated for $g = 880$ nm, while, a small variation of g (±20 nm) leads to an ER_{RR} of about 15 dB). As shown in Fig. 4(a), ER_{RR} is symmetrical with respect to the critical coupling condition, while BW_{RR} follows an inverse exponential trend by varying g (see Fig. 4(b)). Thus, for $g \ll g_{critical}$, ER_{RR} increases and BW_{RR} decreases as g increases, while, for $g \gg g_{critical}$, ER_{RR} decreases and BW_{RR} decreases as g increases. About the phase behaviour (Fig. 4(c)), light travelling within the ring resonator experiences a phase shift of $\angle T_{RR} = -\pi/2$ at $g \equiv g_{critical}$, while, for $g \ll g_{critical}$ and $g \gg g_{critical}$ $\angle T_{RR} = -\pi$ and $\angle T_{RR} = 0$, respectively.

Among the investigated configurations, $R = 15$ μm represents the best compromise between footprint and performance, with maximum

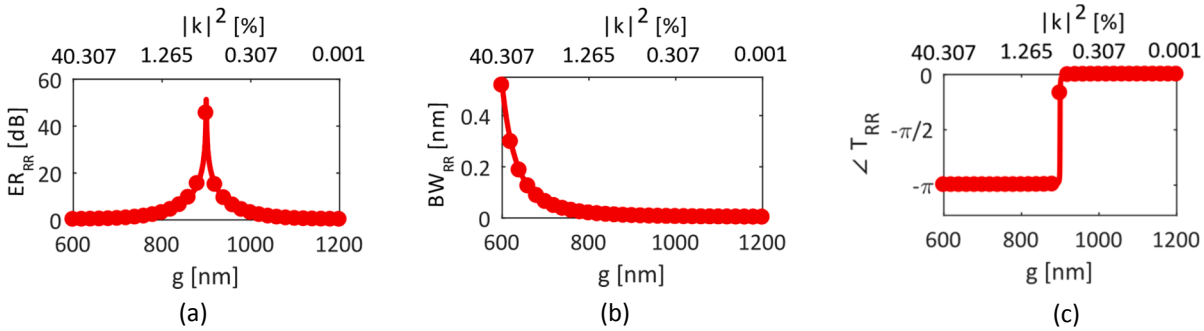

Fig. 4. *ER* (a) *vs. g* ($|k|^2$), *BW* (b) *vs. g* ($|k|^2$), and phase at resonance wavelength at about 1550 nm (c) *vs. g* ($|k|^2$) for $R = 15$ μm. All figures show two *x*-axes: the bottom one represents the coupling gap *g*, while, the top one represents the coupling power efficiency $|k|^2$. Each value of this axis corresponds to a specific value of the coupling gap as derived from Fig. 3.

$ER_{RR} = 51$ dB and $BW_{RR} = 10$ pm at $|k|^2 = K_{critical}$ that corresponds to $g = g_{critical} = 900$ nm. In terms of phase response, for $g \leq 880$ nm, $\angle T_{RR} = 0$, while for $g \geq 980$ nm, $\angle T_{RR} = \pi$. The region near $g_{critical}$ (880 nm $< g <$ 980 nm) will be neglected in the following of the device design, according to the aforementioned remarks about the critical coupling condition.

2.2.2. *CROW load*

The *CROW* loaded on the *MZI* branch (Fig. 2(b)) must be designed according to the performance and operating regions derived for the *RR*, as reported into the Section 2.2.1. As reported in [14], CROW made by two-rings show the frequency degeneration of the resonance related to a single ring resonator, thus, the resonance locking requirement, between the two MZI branches, cannot be fulfilled. Therefore, a three-ring CROW has been designed. The transfer function T_{CROW} of the three-ring CROW is given by:

$$T_{CROW} = \left|\frac{E_{out}}{E_{in}}\right|^2 = \left|\frac{-\tau_1 + \tau_2\Psi + \tau_1\tau_2\tau_3 X + \tau_1\tau_3\Phi - \tau_3\Psi X - \tau_1\tau_2 X\Phi - \tau_2\tau_3\Phi\Psi + \Psi X\Phi}{\tau_1\tau_3\Psi + \tau_2\tau_3 X + \tau_3\Phi - \tau_1\tau_3\Psi X - \tau_2 X\Phi - \tau_1\tau_2\tau_3\Psi\Phi + \tau_1\Psi X\Phi - 1}\right|^2 \quad (2)$$

$$\Psi = e^{i2\pi\beta R_1} \quad X = e^{i2\pi\beta R_2} \quad \Phi = e^{i2\pi\beta R_3}$$

where k_1, k_2, and k_3 are the coupling coefficients referred to the coupling regions with gap g_1, g_2, and g_3, respectively, and $\tau_1 = \sqrt{(1\text{-}k_1^2)}$, $\tau_2 = \sqrt{(1\text{-}k_2^2)}$, and $\tau_3 = \sqrt{(1\text{-}k_3^2)}$ the transmission coefficients. According to the frequency behaviour of three *RRs CROW* [14], the spectrum shows three resonances, whose positions depend on the sum of the *RR* radii and their combinations, according to the numerator in Eq. (2). Central resonance has been assumed as the operating one. To guarantee that the *CROW* response has the same resonance wavelength of the *RR*, the radii of the *CROW* should be multiples or submultiples of *R*: $R_1 = m_1 \cdot R$, $R_2 = m_2 \cdot R$, and $R_3 = m_3 \cdot R$, where m_1, m_2, $m_3 = \ldots, 1/3, 1/2, 1, 2, 3, \ldots$ For the sake of simplicity, we assumed $m_1 = m_2 = m_3 = 1$, and then, $R_1 = R_2 = R_3 = R = 15$ μm. To assess the phase condition, the operating regions where the phase of T_{CROW} at the operating wavelength is equal to π or 0 have been defined.

By using an optimization loop, the spectral response of the *CROW* has been derived by varying g_1, g_2, and g_3, and the 3D contour plot of the extinction ratio, ER_{CROW}, (Fig. 5(a)) and the phase $\angle T_{CROW}$ (Fig. 5(b)) as a function of the triad g_1-g_2-g_3 have been estimated.

Although not easily distinguishable by colours in the light region of the 3D plot in Fig. 5(a), several combinations of g_1-g_2-g_3 provide ER_{CROW} values larger than 100 dB (i.e. for $g_1 = 295$ nm, $g_2 = 310$ nm, $g_3 = 425$ nm, $ER_{CROW} \approx 110$ dB), as denoted by the upper limit of the colorbar in Fig. 5(a). The triad g_1-g_2-g_3 allows also for designing a $\angle T_{CROW}$ that ranges from 0 (green volume) to $\pm\pi$ (blue or yellow volume), (see Fig. 5 (b)).

To define the operating regions that leads to a phase shift of *0* and π, the volume regions have been derived from Fig. 5(b), through 2D relationships between g_1-g_2, g_1-g_3, and g_2-g_3 for $\angle T_{CROW} = 0$ (Fig. 6(a-c)) and $\angle T_{CROW} = \pm\pi$ (Fig. 6(d-f)). As an example, the spectra and phases of the *CROW* with $g_1 = 750$ nm, $g_2 = 655$ nm, $g_3 = 995$ nm (Fig. 7(a,c)) and

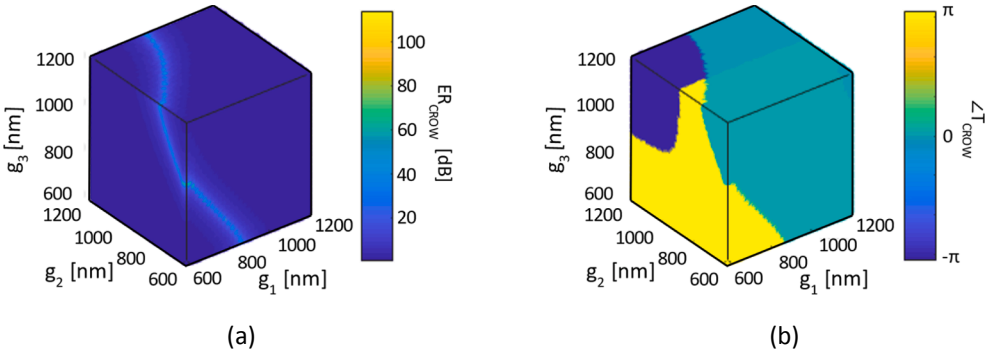

Fig. 5. ER_{CROW} (a) and $\angle T_{CROW}$ (b) 3D contour plots as function of the triad g_1-g_2-g_3.

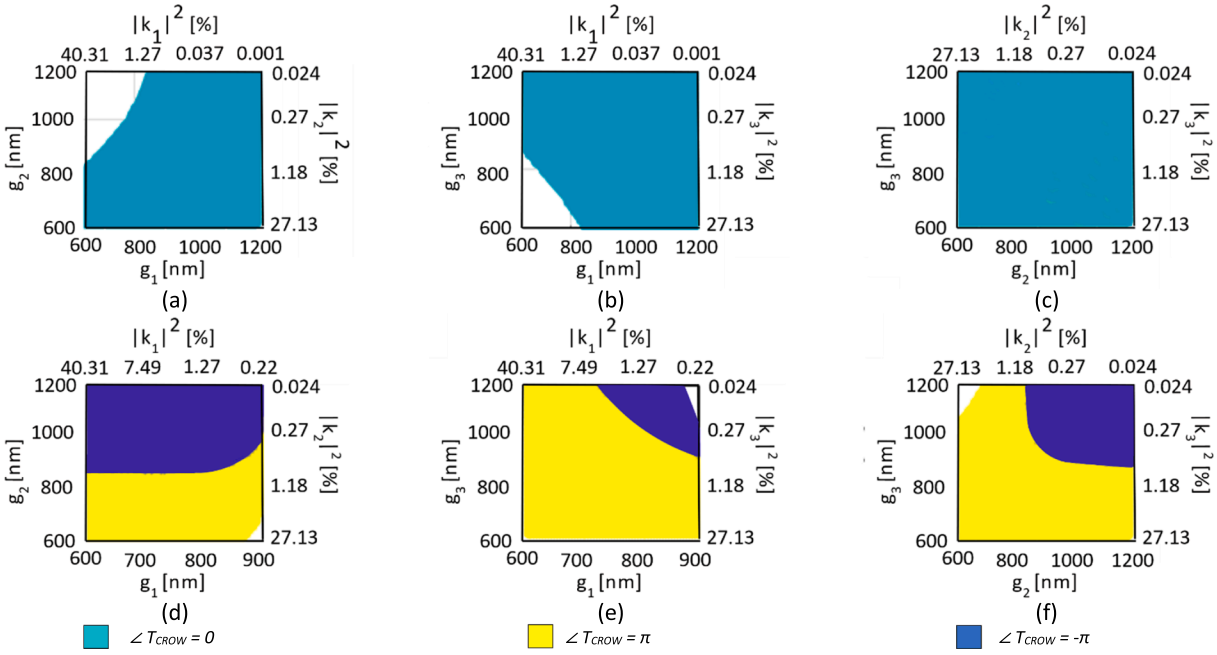

Fig. 6. Surface relationships between g_1 *vs.* g_2, g_1 *vs.* g_3 and g_2 *vs.* g_3 for $\angle T_{CROW} = 0$ (a-c) and $\angle T_{CROW} = \pi$ (d-f). All figures show two *x*-axes and two *y*-axes: each value in the secondary *x* and *y* axes corresponds to a specific value of the coupling gaps.

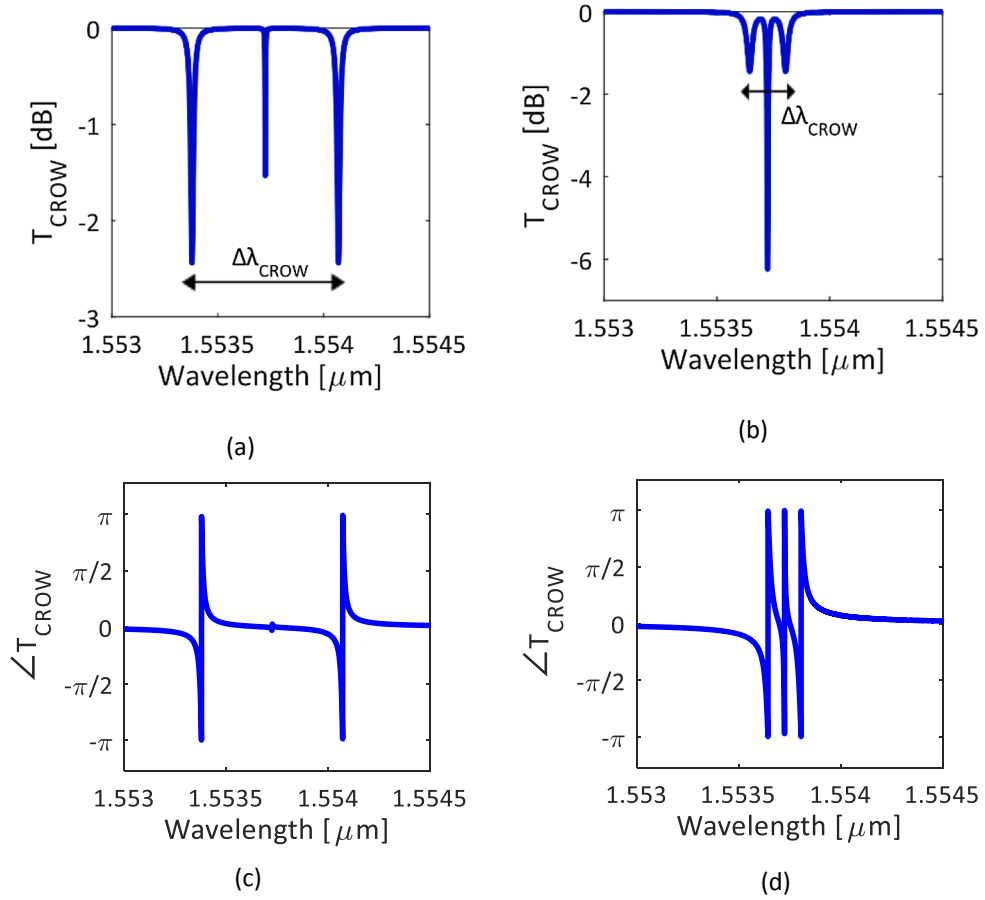

Fig. 7. Power (a) and phase (c) spectra for *CROW* with $g_1 = 750$ nm, $g_2 = 655$ nm, $g_3 = 995$ nm; power (b) and phase (d) spectra for *CROW* with $g_1 = 715$ nm, $g_2 = 845$ nm, $g_3 = 1000$ nm.

$g_1 = 715$ nm, $g_2 = 845$ nm, $g_3 = 1000$ nm (Fig. 7(b,d)) for $\angle T_{CROW} = 0$ and $\angle T_{CROW} = \pm\pi$, respectively, have been evaluated. For both cases, the spectrum shows two extra resonance peaks spaced by $\Delta\lambda_{CROW}$ with same extinction ratio and bandwidth, interleaved by the central resonance.

For $\angle T_{CROW} = 0$ (Fig. 7(a)), the distance between the two extra peaks ($\Delta\lambda_{CROW} \approx 0.69$ nm) is larger than the spectrum with $\angle T_{CROW} = \pi$ ($\Delta\lambda_{CROW} \approx 0.16$ nm), as shown in Fig. 7(b). This behaviour should be taken into account in the *MZI* design to avoid that these resonances could filter components of interest.

3. Numerical results

For the new notch filter, as depicted in Fig. 1, we have achieved very good performance, in terms of *BW* and *ER*. We have modelled the transfer function of the *MZI*, $T_{dualMZI}$:

$$T_{dualMZI} = \left|\frac{E_{out}}{E_{in}}\right|^2 = \left|e^{-\alpha}\left(\frac{1}{2}e^{-\alpha/2}e^{i\beta L_{in}}T_{ring} + \frac{1}{2}e^{-\alpha/2}e^{i\beta L_{in}}T_{crow}\right)\right|^2 \quad (3)$$

where T_{RING} and T_{CROW} are the transfer functions of the *RR* and *CROW*, respectively, L_{in} is the total length of the *MZI* branches (≈ 32 μm) (see Fig. 1(a)), and α is the propagation loss due to the *MMI* [26]. To maximize the performance of the dual-loaded *MZI*, the phase and extinction ratio requirements have to be satisfied.

As before discussed, all ring resonators have the same radius $R = R_1 = R_2 = R_3 = 15$ μm. Furthermore, to meet the *ER* and phase criteria, for 600 nm $< g <$ 880 nm and 920 nm $< g <$ 1300 nm, corresponding to $\angle T_{RING} = 0$ and $\angle T_{RING} = -\pi$, respectively, combinations of g_1-g_2-g_3, that satisfy the condition $\angle T_{CROW} = \pm\pi$ (Fig. 6(a-c)) or $\angle T_{CROW} = 0$ (Fig. 6 (d-f)), respectively, have been identified, through an optimization procedure, aiming at obtaining an *ER* of the *CROW* as close as possible to the *RR* one ($ER_{CROW} \approx ER_{RR}$).

For each value of *g* under investigation, the *CROW* configurations have been identified through the g_1, g_2, and g_3 values and corresponding values of the insertion loss IL_{MZI}, extinction ratio ER_{MZI} and bandwidth BW_{MZI} of the dual-loaded *MZI* have been calculated. Fig. 8 illustrates the performance parameters of the proposed device, ER_{MZI} (Fig. 8(a)) and BW_{MZI} (Fig. 8(b)). The red dots are spaced of 20 nm, and the coupling region not under investigation has been sketched with a grey box.

A dashed red line, as a linear interpolation, clearly defines the *ER* range, with a maximum of about 180 dB and a minimum of 120 dB. Several variations with respect to the linear regression can be observed in Fig. 8(a), due to a non-perfect matching between ER_{RR} and ER_{CROW}, estimated as $|\Delta ER| = |ER_{RR} - ER_{CROW}|$ ($|\Delta ER| \approx 10^{-8}$ in the best case, for $g = 680$ nm, $g_1 = 945$ nm, $g_2 = 655$ nm, and $g_3 = 850$ nm, $|\Delta ER| \approx 10^{-5}$ in the worst case, for $g = 780$ nm, $g_1 = 1015$ nm, $g_2 = 1160$ nm, and $g_3 =$ 935 nm). As shown in Fig. 8(a), ER_{MZI} decreases/increases as *g* increases for 600 nm $< g <$ 880 nm and 920 nm $< g <$ 1300 nm, respectively. A linear trend can be observed up to $g = 1220$ nm, where *ΔER* becomes significant, but with $ER_{CROW} < 0.07$ dB.

BW_{MZI} also shows a symmetrical trend with respect to the coupling conditions, with a quasi-concave parabolic behaviour centred at $g_{critical}$. In terms of *IL* and *BW*, the worst case for $g = 600$ nm shows $BW_{MZI} = 0.05$ nm and $IL_{MZI} = 0.11$ dB. In order to find the best compromise between ER_{MZI} and BW_{MZI}, dual-loaded MZI configurations with $g = 720$ nm, $g_1 = 750$ nm, $g_2 = 655$ nm and $g_3 = 1065$ nm (for $g \ll g_{critical}$) and $g = 1040$ nm, $g_1 = 725$ nm, $g_2 = 980$ nm, $g_3 = 970$ nm (for $g \gg g_{critical}$) have been designed. The spectra of both configurations are reported in Fig. 9. Both spectra show a deep resonance (with $ER_{MZI} = 150$ dB) and two similar extra peaks, symmetrical to the central resonance, (with $ER = 10$ dB), due to the frequency behaviour of the *CROW* (see Fig. 7(a-b)). To avoid that these two extra peaks could filter spectral components of interest, an additional design criterion must be considered: BW_{RR} should be larger or, in the worst case, comparable with the spectral distance $\Delta\lambda_{CROW}$.

The presence of extra peaks in the *MZI* spectrum has been investigated, also, referring to *ER* (ER_{peaks}). Several configurations do not show extra peaks for $g \ll g_{critical}$, in contrast to all configurations for $g \gg g_{critical}$ where the condition $BW_{RR} \ll \Delta\lambda_{CROW}$ leads to the creation of undesired extra peaks. This behaviour strictly depends on the variation of BW_{RR} with *g*. Among the cases without extra peaks, the configuration with $g = 640$ nm, $g_1 = 1160$ nm, $g_2 = 1190$ nm and $g_3 = 725$ nm, and $R = R_1 = R_2 = R_3 = 15$ μm represents the best compromise in terms of *IL*, *BW* and *ER*. In particular, $ER_{MZI} = 150.55$ dB, $IL_{MZI} = 0.104$ dB and $BW_{MZI} = 0.243$ nm have been calculated (Fig. 10), within a footprint of ≈ 60 μm × 160 μm. To our knowledge, this performance represents a significant improvement of the state-of-the-art of pump rejection filters for quantum photonic systems.

4. Tunability of the new device

The thermo-optic tuning is the physical effect we have considered in our design to make flexible the filtering function. The spectral response can be shifted by applying an electrical power to the electrodes distributed along a specific region of the ring resonators (Fig. 1(a)).

The geometry and position of electrodes must be properly identified to avoid any impact on the coupling efficiency. Electrodes are placed along the ring outside the coupling regions. Furthermore, in order to ensure a same shift of the resonance in all ring resonators, the ring regions subjected to an effective index change induced by the thermo-optical tuning, should be the same for all *RR*s. The coupling region has been supposed as the region delimited by a coupling gap 10 times larger than the minimum one, where the coupling efficiency is null [33].

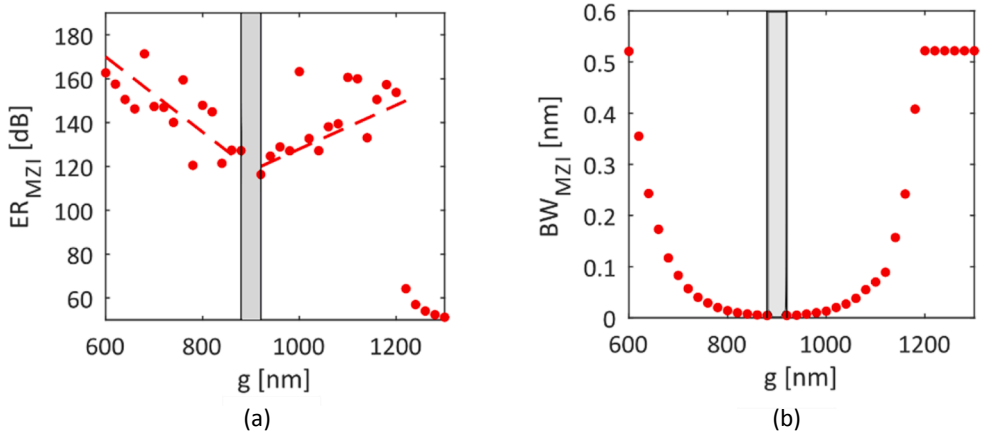

Fig. 8. ER_{MZI} (a) and BW_{MZI} (b) of the designed dual loaded *MZI*.

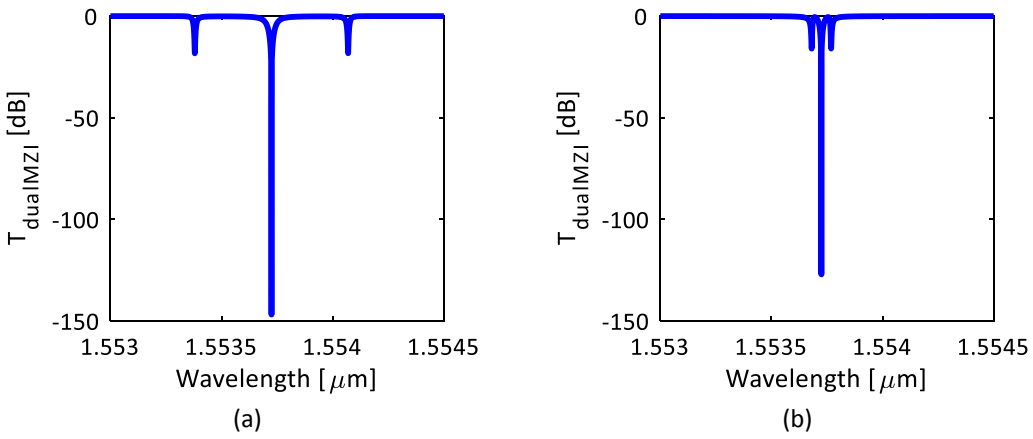

Fig. 9. Spectra of dual-loaded *MZI* $g = 720$ nm, $g_1 = 750$ nm, $g_2 = 655$ nm and $g_3 = 1065$ nm (a) and $g = 1040$ nm, $g_1 = 725$ nm, $g_2 = 980$ nm, $g_3 = 970$ nm (b).

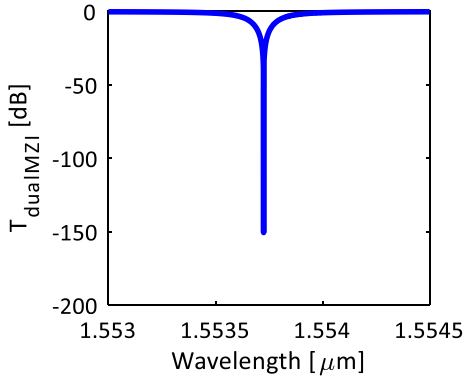

Fig. 10. Transmission spectrum of the designed dual-loaded *MZI* with $g = 640$ nm, $g_1 = 1160$ nm, $g_2 = 1190$ nm and $g_3 = 725$ nm and $R = R_1 = R_2 = R_3 = 15$ μm.

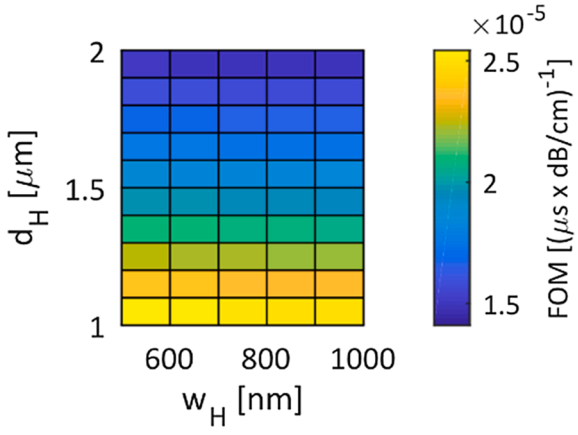

Fig. 12. Contour plot of *FOM vs.* $d_H - w_H$.

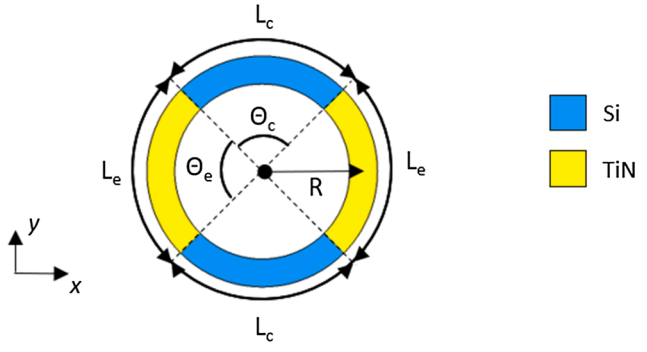

Fig. 11. Top view of a ring resonator with *TiN* electrodes, where L_c is the coupling region length, L_e is the length of electrode, Θ_c is the angular sector related to the coupling region, Θ_c is the angular sector related to the electrodes. All *RRs* of the designed device show the same electrodes configuration. The interleaved silica layer between the ring resonator and the electrodes is not shown in figure.

The electrode lengths correspond to the ring resonator path outside the largest coupling region with gap g_2 for the designed dual-loaded *MZI*. Hence, since $g_2 = 1190$ nm entails a coupling region with an angular sector $\Theta_c = 108°$ for radii of 15 μm, the electrodes are distributed along an angular section $2\Theta_e = 144°$ of all ring resonators (see Fig. 11). Each electrode has a length $L_e = 37.7$ μm and both of them are placed symmetrically with respect to the coupling regions.

The thermo-optic behaviour of the structure sketched in Fig. 1(c) has been simulated by using a 3D-*FEM* approach, by combining a thermal solver and an optical mode solver, to analyze the heat distribution, the efficiency and the transient response. The metal chosen for the electrode is Titanium Nitride (TiN), thanks to its properties of high hardness, high corrosion resistance and thermal and chemical stability [34]. The heater t_H thick and w_H wide is placed on top of the waveguide at a distance d_H from the silicon core. According to [34], the thickness t_H has been assumed equal to 100 nm. From FEM simulations, the d_H values larger than 1 μm minimize the excess loss due to the presence of metal layer on the waveguide.

The final values of d_H and w_H have been designed by finding the best compromise in terms of tuning loss α_t, time response τ_r and tuning efficiency, expressed through the effective refractive index change Δn. By

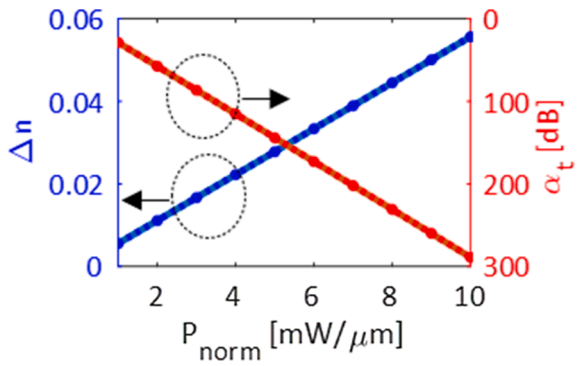

Fig. 13. Δn (blue curve) and α_t (red curve) trends by varying P_{norm}.

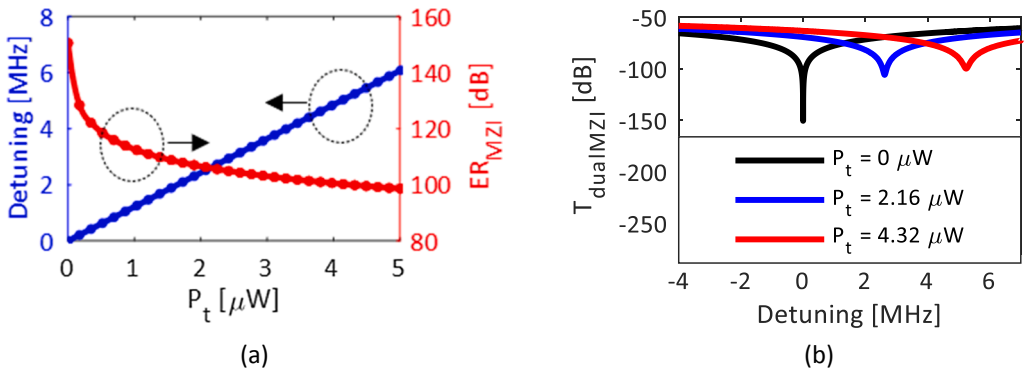

Fig. 14. (a) Detuning (blue curve) and ER_{MZI} (red curve) trends by varying P_t; (b) transmission spectra of the dual-loaded *MZI* for several values of P_t.

considering an input electrical power, normalized with respect to the electrode length, $P_{norm} = 0.5$ mW/μm, the best w_H - d_H combination has been obtained by optimizing the figure of merit $FOM = \Delta n / (\tau_r \cdot \alpha_t)$ [(μs × dB/cm)$^{-1}$] (Fig. 12).

The combination $d_H = 1000$ nm - $w_H = 500$ nm leads to the highest value of $FOM = 2.55 \times 10^{-5}$ (μs × dB/cm)$^{-1}$, with $\tau_r \approx 8$ μs and $\alpha_t \approx 100$ dB/cm. Moreover, the impact of the normalized input power P_{norm} on the performance has been evaluated (Fig. 13). Once defined the total electrodes length and derived the Δn *vs.* P_{norm} and α_t *vs.* P_{norm} relationships from Fig. 12, the shift with respect to the resonance wavelength without tuning and ER_{MZI} as a function of the tuning power P_t, have been evaluated (Fig. 14(a)). The detuning increases as input power increases, worsening the value of ER_{MZI}, due to an increase of the tuning losses α_t (Fig. 13) that raises the extinction ratio mismatch between *RR* and *CROW*, being the tuning losses of *CROW* devices 3 times larger than the RR one. A maximum detuning equal to 6 MHz, corresponding to $P_t = 4.32$ μW, has been achieved, with an ER_{MZI} equal to 100 dB in the worst case, as shown in the dual-loaded *MZI* response in Fig. 14(b). With the same tuning power ($P_t = 4.32$ μW), we have calculated $BW = 0.244$ nm and $IL = 0.21$ dB, which still satisfy the system requirements, demonstrating in this way the feasibility of the filter response tuning.

5. Conclusions

In this paper, we have proposed the design of an ultra-compact high performance silicon-on-insulator pump-rejection filter with large suppression ratio, narrow bandwidth and low insertion losses, to be used to preserve the single-photon pair in photonic quantum system. The proposed device consists of a dual-loaded *MZI*, with a ring resonator and a three *RR* CROW, distinctly loaded on the *MZI* branches. The designed filter exhibits an extinction ratio of 150.55 dB, insertion loss of 0.104 dB and rejection bandwidth of 0.243 nm, within a footprint of ≈ 60 μm × 160 μm. The tunability of the proposed device has been also demonstrated, with a maximum detuning of about 6 MHz, a worst extinction ratio of about 100 dB and a time response of about 8 μs.

To our knowledge, the performance of proposed device represents a remarkable improvement of the state-of-the-art, in terms of extinction ratio, insertion loss, bandwidth and footprint, along with effective tuning possibilities. The device guarantees large suppression of the pump signal in a wide range photonic systems for quantum information processing purposes, also allowing the reduction of the observation time and ensuring the capability to manage short signal-idler separation, thus, improving the *SFWM* efficiency.

Declaration of Competing Interest

The authors declare that they have no known competing financial interests or personal relationships that could have appeared to influence the work reported in this paper.

Acknowledgments

This work is supported by Ministry of Research and University in the framework of New Satellites Generation components (NSG) project (no. ARS_01_01_2015).

References

[1] C. Monroe, Quantum information processing with atoms and photons, Nature 416 (6877) (2002) 238–246, https://doi.org/10.1038/416238a.
[2] P. Kok, B.W. Lovett, Introduction to optical quantum information processing, Cambridge University Press (2010), https://doi.org/10.1017/CBO9781139193658.
[3] R. Raussendorf, H.J. Briegel, A one-way quantum computer, Phys. Rev. Lett. 86 (22) (2001) 5188, https://doi.org/10.1103/PhysRevLett.86.5188.
[4] A. Politi, J.C. Matthews, M.G. Thompson, J.L. O'Brien, Integrated quantum photonics, IEEE J. Sel. Top. Quantum Electron. 15 (6) (2009) 1673–1684, https://doi.org/10.1109/JSTQE.2009.2026060.
[5] G. Masada, K. Miyata, A. Politi, T. Hashimoto, J.L. O'Brien, A. Furusawa, Continuous-variable entanglement on a chip, Nat. Photonics 9 (5) (2015) 316–319, https://doi.org/10.1038/nphoton.2015.42.
[6] A. Politi, M.J. Cryan, J.G. Rarity, S. Yu, J.L. O'Brien, Silica-on-silicon waveguide quantum circuits, Science 320 (5876) (2008) 646–649, https://doi.org/10.1126/science.1155441.
[7] S. Azzini, D. Grassani, M.J. Strain, M. Sorel, L.G. Helt, J.E. Sipe, M. Liscidini, M. Galli, D. Bajoni, Ultra-low power generation of twin photons in a compact silicon ring resonator, Opt. Express 20 (21) (2012) 23100–23107, https://doi.org/10.1364/OE.20.023100.
[8] F. Mazeas, M. Traetta, M. Bentivegna, F. Kaiser, D. Aktas, W. Zhang, C.A. Ramos, L. Ngah, T. Lunghi, E. Picholle, N. Belabas-Plougonven, X. Le Roux, E. Cassan, D. Marris-Morini, L. Vivien, G. Sauder, L. Labontè, S. Tanzilli, High-quality photonic entanglement for wavelength-multiplexed quantum communication based on a silicon chip, Opt. Express 24 (25) (2016) 28731–123738, https://doi.org/10.1364/OE.24.028731.
[9] L.G. Helt, Z. Yang, M. Liscidini, J.E. Sipe, Spontaneous four-wave mixing in microring resonators, Opt. Lett. 35 (18) (2010) 3006–3008, https://doi.org/10.1364/OL.35.003006.
[10] M. Pieikarek, D. Bonneau, S. Miki, T. Yamashita, M. Fujiwara, M. Sasaki, H. Terai, M.G. Tanner, C.M. Natarajan, R.H. Hadfield, J.L. O'Brien, M.G. Thompson, High-extinction ratio integrated photonic filters for silicon quantum photonics, Opt. Lett. 42 (4) (2017) 815–818, https://doi.org/10.1364/OL.42.000815.
[11] J.C. Matthews, A. Politi, A. Stefanov, J.L. O'Brien, Manipulation of multiphoton entanglement in waveguide quantum circuits, Nat. Photonics 3 (6) (2009) 346–350, https://doi.org/10.1038/nphoton.2009.93.
[12] E. Engin, D. Bonneau, C.M. Natarajan, A.S. Clark, M.G. Tanner, R.H. Hadfield, S. N. Dorenbos, V. Zwiller, K. Ohira, N. Suzuki, H. Yoshida, N. Iizuka, M. Ezaki, J. L. O'Brien, M.G. Thompson, Photon pair generation in a silicon micro-ring resonator with reverse bias enhancement, Opt. Express 21 (23) (2013) 27826–27834, https://doi.org/10.1364/OE.21.027826.
[13] N. Matsuda, P. Karkus, H. Nishi, T. Tsuchizawa, W.J. Munro, H. Takesue, K. Yamada, On-chip generation and demultiplexing of quantum correlated photons using a silicon-silica monolithic photonic integration platform, Opt. Express 22 (19) (2014) 22831–22840, https://doi.org/10.1364/OE.22.022831.
[14] G. Brunetti, M.N. Armenise, C. Ciminelli, Silicon-based optical-pump rejection filter for quantum photonics, in: in 22nd International Conference on Transparent Optical Networks (ICTON), 2020, https://doi.org/10.1109/ICTON51198.2020.9203536.
[15] C. Harris, D. Grassani, A. Simbula, M. Pant, M. Galli, T. Baehr-Jones, M. Hochberg, D. Englund, D. Bajoni, C. Galland, Integrated source of spectrally filtered correlated photons for large-scale quantum photonic systems, Phys. Rev. X 4 (4) (2014), 041047, https://doi.org/10.1103/PhysRevX.4.041047.
[16] D. Pérez-Galacho, C. Alonso-Ramos, F. Mazeas, X. Le Roux, D. Oser, W. Zhang, D. Marris-Morini, L. Labontè, S. Tanzilli, E. Cassan, L. Vivien, Optical pump-

rejection filter based on silicon sub-wavelength engineered photonic structures, Opt. Lett. 42 (8) (2017) 1468–1471, https://doi.org/10.1364/OL.42.001468.
[17] C. Alonso-Ramos, A. Ortega-Monux, I. Molina-Fernandez, A. Annoni, A. Melloni, M. Strain, M. Sorel, P. Orlandi, P. Bassi, and F. Morichetti, "Silicon-on-insulator single channel-extraction filter for DWDM applications," in Proc. IEEE 11th International Conference on Group IV Photonics (GFP), 219-220, 2014, DOI: 10.1109/Group4.2014.6961933.
[18] D. Oser, F. Mazeas, C. A. Ramos, X. Le Roux, L. Vivien, S. Tanzilli, E. Cassan, and L. Labontè, "On-chip photon pair source with pump rejection filter," in Proc. IEEE 2019 Conference on Lasers and Electro-Optics Europe & European Quantum Electronics Conference (CLEO/Europe-EQEC), 1, 2019, DOI: 10.1109/CLEOE-EQEC.2019.8872272.
[19] M. Qiu, M. Mulot, M. Swillo, S. Anand, B. Jaskorzynska, A. Karlsson, M. Kamp, A. Forchel, Photonic crystal optical filter based on contra-directional waveguide coupling, Appl. Phys. Lett. 83 (25) (2003) 5121–5123, https://doi.org/10.1063/1.1634373.
[20] A. Afifi, L. Chrostowski, M. Hammood, N. A. Jaeger, S. Shekkar, and J. F. Young, "Contra-directional couplers as pump rejection and recycling filters for on-chip photon-pair sources," in Proc. IEEE 16th International Conference on Group IV Photonics (GFP), vol. 1949, pp. 1-2, 2019, DOI: 10.1109/GROUP4.
[21] X. Nie, N. Turk, Y. Li, Z. Liu, R. Baets, High extinction ratio on-chip pump-rejection filter based on cascaded grating-assisted contra-directional couplers in silicon nitride rib waveguides, Opt. Lett. 44 (9) (2019) 2310–2313, https://doi.org/10.1364/OL.44.002310.
[22] C.M. Wilkes, X. Qiang, J. Wang, R. Santagati, S. Paesani, X. Zhou, D.A.B. Miller, G. D. Marshall, M.G. Thompson, J.L. O'Brien, 60 dB high-extinction auto-configured Mach-Zehnder interferometer, Opt. Lett. 41 (22) (2016) 5318–5321, https://doi.org/10.1364/OL.41.005318.
[23] R.R. Kumar, X. Wu, H.K. Tsang, Compact high-extinction tunable CROW filters for integrated quantum photonic circuits, Opt. Lett. 45 (6) (2020) 1289–1292, https://doi.org/10.1364/OL.384187.
[24] R. M. Knox, and P. P. Toulios, "Integrated circuits for the millimeter through optical frequency range," in Proc. Symp. Submillimeter Waves, vol. 20, 1970.
[25] S. K. Selvaraja, P. De Heyn, G. Winroth, P. Ong, G. Lepage, C. Cailler, A. Rigny, K. K. Bourdelle, W. Bogaerts, D. Van Thouhout, J. Van Campenhout, and P. Absil, "Highly uniform and low-loss passive silicon photonics devices using a 300mm CMOS platform," in Proc. OSA Optical Fiber Communication Conference, pp. Th2A-33, 2014, DOI: 10.1364/OFC.2014.
[26] Z. Sheng, Z. Wang, C. Qiu, L. Li, A. Pang, A. Wu, X. Wang, S. Zou, F. Gan, A compact and low-loss MMI coupler fabricated with CMOS technology, IEEE Photonis J. 4 (6) (2012) 2272–2277, https://doi.org/10.1109/JPHOT.2012.2230320.
[27] Y.A. Vlasov, S.J. McNab, Losses in single-mode silicon-on-insulator strip waveguides and bends, Opt. Express 12 (8) (2004) 1622–1631, https://doi.org/10.1364/OPEX.12.001622.
[28] M. Harjanne, M. Kapulainen, T. Aalto, P. Heimala, Sub-μs Switching Time in Silicon-on-Insulator Mach– Zehnder Thermooptic Switch, IEEE Photonics Technol. Lett. 16 (9) (2004) 2039–2041, https://doi.org/10.1109/LPT.2004.833896.
[29] M.W. Geis, S.J. Spector, R.C. Williamson, T.M. Lyszczarz, Submicrosecond submilliwatt silicon-on insulator thermooptic switch, IEEE Photonics Technol. Lett. 16 (11) (2004) 2514–2516, https://doi.org/10.1109/LPT.2004.835194.
[30] G. Brunetti, F. Dell'Olio, D. Conteduca, M.N. Armenise, C. Ciminelli, Ultra-compact tuneable notch filter using silicon photonic crystal ring resonator, J. Lightwave Technol. 37 (13) (2019) 2970–2980, https://doi.org/10.1109/JLT.2019.2908364.
[31] J. Van Roey, J. Van der Donk, P.E. Lagasse, Beam-propagation method: analysis and assessment, Josa 71 (7) (1981) 803–810, https://doi.org/10.1364/JOSA.71.000803.
[32] A. Yariv, Critical coupling and its control in optical waveguide-ring resonator systems, IEEE Photonics Technol. Lett. 14 (4) (2002) 483–485, https://doi.org/10.1109/68.992585.
[33] F. Dell'Olio, D. Conteduca, C. Ciminelli, M.N. Armenise, New ultrasensitive resonant photonic platform for label-free biosensing, Opt. Express 23 (22) (2015) 28593–28604, https://doi.org/10.1364/OE.23.028593.
[34] Europractice MPW Prototyping, Si-Photonics (http://europractice-ic.com/mpw-prototyping/siphotonics/).